NANO LETTERS

2008
Vol. 8, No. 5
1393-1398

A Unified Description of Current–Voltage Characteristics in Organic and Hybrid Photovoltaics under Low Light Intensity

R. A. Marsh,* C. R. McNeill, A. Abrusci, A. R. Campbell, and R. H. Friend

Cavendish Laboratory, J. J. Thomson Avenue, Cambridge CB3 0HE, United Kingdom

Received January 21, 2008; Revised Manuscript Received March 5, 2008

ABSTRACT

We develop a simple model that can explain the current–voltage ($J-V$) curves of excitonic photovoltaic solar cells, spanning polymer:polymer, polymer:fullerene, and polymer:nanocrystal devices. We show that by subtracting out the dark current, we can explain apparent intensity-dependent characteristics and thus identify geminate recombination as the dominant loss mechanism and establish its electric field dependence. We present an analytic fit to the $J-V$ curves of all measured devices based on a single fitted parameter, the electric field required to split 50% of geminate charge pairs, which we term the critical field. Devices of different material combinations and morphologies can all be described by this method and yield critical fields varying between >1 $\times$ 10^8 V/m for blends of poly(9,9′-dioctylfluorene-*co*-bis-*N*,*N*′-(4-butylphenyl)-bis-*N*,*N*′-phenyl-1,4-phenylenediamine) (PFB) and poly(9,9′-dioctylfluorene-*co*-benzothiadiazole) (F8BT) and 8 $\times$ 10^5 V/m for slow-grown blends of poly(3-hexylthiophene-2,5-diyl) (P3HT) and [6,6]-phenyl-C61-butyric acid methyl ester (PCBM). A comparison with material properties reveals that the primary route to improved photovoltaic materials is enhanced charge delocalization.

Organic semiconductors have great potential to produce affordable photovoltaic energy.[1–3] However, owing to the low dielectric constant of such materials, photoexcitation forms a bound electron–hole pair (exciton). Excitons can be dissociated efficiently at the interface between two materials of different electron affinities (termed the heterojunction), however this generally results in a bound charge-transfer state. Subsequent separation of these bound geminate pairs requires that they overcome their Coulombic attraction and thus avoid recombination.

It has been shown that heterojunctions as diverse as polymer:polymer,[4,5] polymer:fullerene,[6] and polymer:nanocrystal[7] can support photocurrent generation. A great challenge in the search for improved photovoltaic efficiency is identifying why certain material combinations give superior performance and hence guiding the design of future materials. Therefore, we seek here to understand the $J-V$ characteristics of photovoltaic cells based on a variety of different material combinations. The materials used include polymers, poly(9,9′-dioctylfluorene-*co*-bis-*N*,*N*′-(4-butylphenyl)-bis-*N*,*N*′-phenyl-1,4-phenylenediamine) (PFB), poly(9,9′-dioctylfluorene-*co*-benzothiadiazole) (F8BT), poly(3-hexylthiophene-2,5-diyl) (P3HT), and poly((9,9-dioctylfluorene)-2,7-diyl-*alt*-[4,7-bis(3-hexylthien-5-yl)-2,1,3-benzothiadiazole]-2′,2″-diyl) (F8TBT), molecules, [6,6]-phenyl-C61-butyric acid methyl ester (PCBM), and nanocrystals, CdSe nanorods. Details of device manufacture are given in the Experimental Section. We find that the short-circuit current, (J_{SC}), is directly proportional to intensity in all cases. At all other biases, positive and negative, we find the total current is not proportional to intensity, giving an intensity dependence of the fill factor (FF) and open-circuit voltage (V_{OC}), see Figure 1. It should be noted that the extent and functional form of this intensity dependence vary widely across the different device types measured.

To understand these observations, we identify the two contributions to measured $J-V$ curves. First, photocurrent arises from photogenerated excitons dissociating across a heterojunction, the separation of resulting carriers, and extraction at opposite electrodes. Second, dark current results from carriers injected from one or both electrodes into the device film. It is reasonable to assume that these two current contributions do not significantly interact, particularly under low-light intensity.[8] Therefore, we propose that the net photocurrent may be determined by subtracting the dark current:

$$J_{light}(V) = J_T(V) - J_{dark}(V) \quad (1)$$

where J_T denotes measured total current density, V applied voltage, and J_{light} and J_{dark} are the contributions from photoexcited carriers and carriers injected at the electrodes, respectively.

* Corresponding author. E-mail: ram47@cam.ac.uk.

10.1021/nl080200p CCC: $40.75
Published on Web 03/26/2008

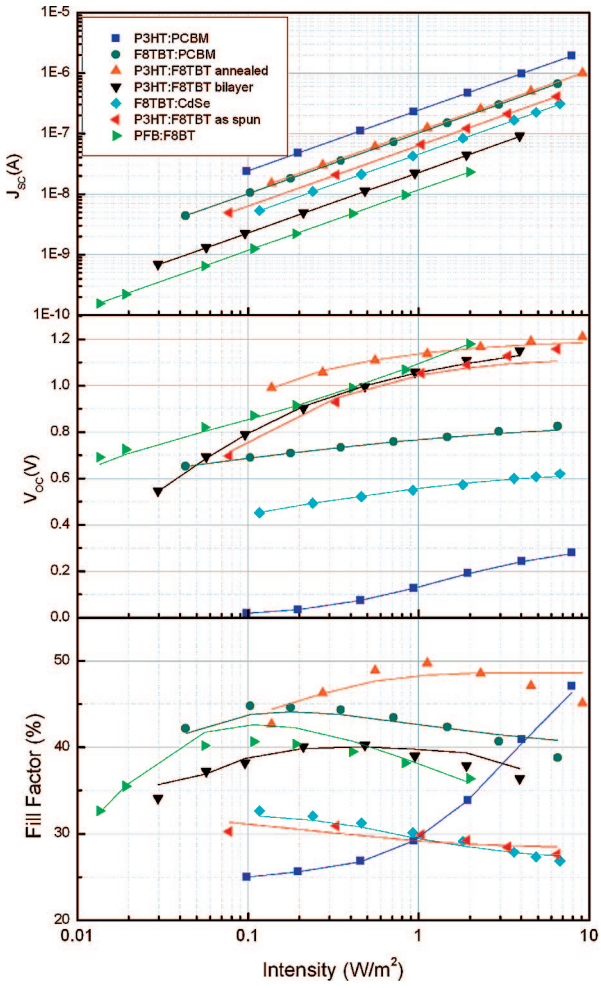

Figure 1. Intensity dependence of short-circuit current, open-circuit voltage, and fill factor. Solid symbols represent measured values for a variety of different devices, and lines represent fits using eq 6. Devices were illuminated with monochromatic light, the wavelength chosen to optimize absorption in each case. For measurement wavelengths and device preparation details, see Experimental Section.

To isolate the behavior of geminate pairs at the heterojunction, we restrict our measurements to low light intensities. A discussion of higher light intensity effects follows later in the letter. It is known that these geminate pairs can be initially strongly Coulombically bound, being generated directly across the heterojunction following exciton dissociation. Several recombination channels exist, including direct to the ground state, via a triplet exciton[9] or even radiatively via an exciplex.[10] Successful separation of these geminate pairs requires that they overcome their Coulombic attraction before decaying by any of these channels. We find that the net photocurrent, $J_{light}(V)$, depends linearly on intensity over 2 orders of magnitude for all devices tested. This indicates that the dominant loss mechanism in the devices is unimolecular. This excludes bimolecular recombination of mobile charges and space charge effects. Given the low dielectric constant of these materials and hence high Coulombic binding energy of geminate charge pairs across the heterojunction, we conclude that geminate recombination is the most likely unimolecular loss mechanism. Hence our results

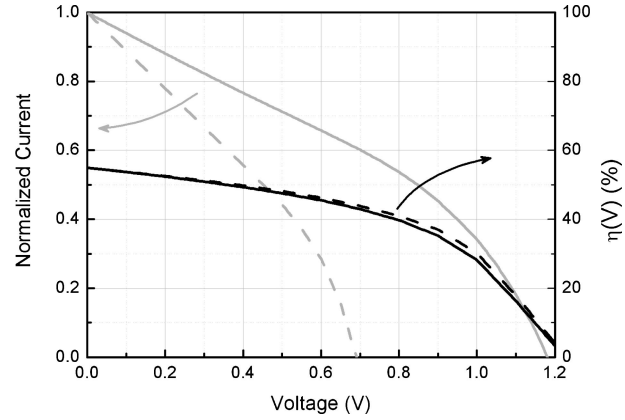

Figure 2. P3HT:F8TBT postannealed device: intensity dependent $J-V$ and $\eta(V)$ curves measured under light intensities of 0.1 (dashed lines) and 9 W/m^2 at a wavelength of 550 nm (solid lines). $J-V$ curves (gray) are normalized to short-circuit. For device preparation details, see Experimental Section. Note that V_0 is given by $\eta(V_0) = 0$, here 1.25 V. A discussion of device behavior under higher incident light intensities follows later in the letter.

suggest that photocurrent generation depends only on the competition between separation and recombination of geminate pairs:

$$J_{light}(V) = I \times e \times \eta(V) \quad (2)$$

Here, I denotes the incident photon flux, e the charge of an electron, and $\eta(V)$ denotes the empirically determined voltage dependence of the quantum efficiency. Figure 2 contrasts the strong intensity dependence of the total measured current with the intensity independence of $\eta(V)$.

By subtracting the dark current, we therefore easily understand the light intensity dependence of all tested devices' $J-V$ curves. At low light intensities, the net photocurrent generated is smaller, and therefore the dark current is proportionally more significant. The open-circuit voltage should be understood as the voltage at which the opposite dark and light current contributions balance. It therefore falls dramatically under lower light intensities as the photocurrent is reduced. It is incorrect to suppose that the open-circuit voltage is a measurement of the built-in potential. Instead, this potential is best determined by measuring the voltage at which net photocurrent generation is zero. It should be noted that all experimental trends here are adequately explained by considering only geminate pair dynamics, without the need to invoke more complex arguments. These include drift-diffusion equations,[11–14] bimolecular recombination,[15,16] and space-charge effects.[17,18]

We have identified the importance of geminate pair dynamics in determining the light intensity and voltage dependence of net photocurrent in a wide variety of devices. We now seek the simplest model that encapsulates the competition between geminate pair recombination with rate $k_r(F)$ and separation with rate $k_s(F)$. We suppose that recombination is approximately independent of electric field, F, so that $k_r(F) = \nu_r$, where ν_r is the characteristic rate constant for recombination of geminate pairs across the heterojunction. Conversely, separation is undoubtedly strongly field-dependent, and we take the lowest order term in the

Taylor expansion of $k_s(F)$. It should be noted that we do not assume a theoretical formula for $k_s(F)$ at this stage but take the most general expression that is physically reasonable. Because we are measuring charges that escape recombination and are collected as photocurrent, the process $k_s(F)$ also describes movement of free charges to opposite electrodes. Therefore the lowest order term of $k_s(F)$ cannot in general be zero order because we must consider carrier diffusion subsequent to geminate pair dissociation. Isotropic morphologies such as blends have no directionality and must therefore yield zero net photocurrent under zero electric field. In fact, the absence of directionality implies that $k_s(F)$ must be an odd function. Hence, the lowest nonzero term is linear in electric field, $k_s(F) = \nu_s F$. We can now model the quantum efficiency $\eta(F)$ in terms of the branching ratio between geminate pair recombination and separation followed by collection at opposite electrodes:

$$\eta(F) \propto \frac{k_s(F)}{k_s(F) + k_r(F)} \tag{3}$$

$$\propto \frac{\nu_s F}{\nu_s F + \nu_r} \tag{4}$$

$$F = \frac{V_0 - V}{d} \tag{5}$$

where V_0 is the built-in field in the device owing to the different electrodes' workfunctions. This, the first parameter of the model, is not free to vary, but fixed as the voltage corresponding to zero net photocurrent generation.

The second parameter of the model is the constant of proportionality in eq 4. This is equal to $\eta_A \times \eta_{ED}$, where η_A is the light absorption efficiency at the appropriate wavelength, and η_{ED} is the fraction of excitons that diffuse to a heterojunction and dissociate there to form a geminate charge pair. It is in general difficult to measure η_A owing to internal reflections at the top electrode.[19] However, we can obtain a reasonable estimate from our experimentally determined function $\eta(F)$. Under reverse bias, the geminate pair separation efficiency tends toward unity, and so $\eta(F)$ tends toward $\eta_A \times \eta_{ED}$. Therefore this parameter too is well constrained by the experimental data.

The third and final parameter of the model is the ratio between ν_r and ν_s, which has the dimensions of an electric field. We term this the critical field, $F_c = \nu_r/\nu_s$, such that

$$\eta(F) = \eta_A \times \eta_{ED} \frac{F}{F + F_c} \tag{6}$$

Hence F_c is the electric field required to split 50% of geminate pairs. This parameter is freely fitted to describe the electric field dependence of geminate pair separation in each device.

Remarkably, we find that this model is able to describe the $J-V$ characteristics of all devices investigated. We can therefore account for the intensity dependence of I_{SC}, FF, and V_{OC} when in the low light intensity regime, Figure 1. The values of the three parameters, V_0, $\eta_A \times \eta_{ED}$, and F_c are presented in Table 1. The fact that this treatment describes geminate pair dynamics in such a wide range of material systems is surprising and indicates that these different heterojunction types may have more in common than previously recognized.

Table 1. V_0, $\eta_A \times \eta_{ED}$, and F_c, Extracted from $J-V$ Curve Fits for Blends of Different Material Combinations and Morphologies[a]

material combination	V_0 (V)	$\eta_A \times \eta_{ED}$ (%)	F_c (10^6V/m)
F8TBT:P3HT (annealed)	1.2 ± 0.05	40 ± 5	6 ± 2
F8TBT:P3HT (as spun)	1.15 ± 0.05	>70	80 ± 30
F8TBT:P3HT (bilayer)	1.2 ± 0.05	40 ± 5	11 ± 2
F8BT:PFB	1.3 ± 0.05	>10	>100
F8TBT:PCBM	0.85 ± 0.05	55 ± 5	2.7 ± 0.75
P3HT:PCBM	0.4 ± 0.05	65 ± 5	0.8 ± 0.4
F8TBT:CdSe	0.6 ± 0.05	50 ± 5	23 ± 6

[a] The first two parameters are well-constrained by experimental results, and the third is freely fitted.

Here we have confined our analysis to low light intensities to isolate the behavior of geminate pairs. Under higher light intensities, it is possible that additional effects such as charge-density dependence of mobilities, bimolecular recombination, or space-charge may also play a role. It has been shown that space-charge effects tend to dominate when charge transport is highly unbalanced[20] and bimolecular recombination becomes significant where mobilities are low, resulting in high charge density.[16] However, it is generally found that more efficient solar cells exhibit linear net photocurrent generation even up to AM1.5 conditions, indicating that geminate pair dynamics remain of key importance. This is already documented in the case of the most efficient of the devices investigated, slow-grown P3HT:PCBM[20] and annealed P3HT:F8TBT,[5] and we find our analysis reproduces their efficiencies under such conditions to within 10%. Therefore, design rules obtained from this model for further improvements remain pertinent up to AM1.5 conditions.

Of the three model parameters, the first two are well constrained by the experimental data, and the last, F_c, is freely fitted. It can be seen from Table 1 that the built-in potential V_0 ranges between 0.4 and 1.3 V. The two polymer:fullerene combinations both exhibit lower built-in potentials, as does the polymer:nanocrystal device. We note that the P3HT:PCBM devices presented elsewhere have exhibited slightly superior open-circuit voltages, approaching 0.6 V,[6] and hence the figure here should not be taken as the optimum possible for this material combination. The four polymer:polymer devices all have very similar built-in potentials around 1.2 V. A number of factors have been proposed to determine the built-in potential. These include the energy level alignment of the two semiconducting materials, the Fermi levels of the two electrodes used,[21] and surface chemistry effects between the electrodes and the semiconductors. In this study, indium tin oxide (ITO) and aluminum were used as the electrodes in all cases, so the second of these factors can be ruled out. We identify that the lowest built-in potentials correspond to those material combinations in which the electron acceptor has the lowest LUMO (lowest unoccupied molecular orbital): PCBM and CdSe nanocrystals. This suggests that choosing electron-acceptors with higher LUMO levels may help increase the built-in potential in organic photovoltaic devices, as has been demonstrated recently elsewhere.[22] Because we are primarily concerned

with geminate charge pair dynamics here, we do not address the origin of the built-in potential in any more detail.

The second parameter, $\eta_A \times \eta_{ED}$, is comparable for all devices with a blend morphology. We observe that annealing of the P3HT:F8TBT device reduces this quantity somewhat, which may result from increasing domain size in the blend. The bilayer exhibits the lowest value of $\eta_A \times \eta_{ED}$, which is consistent with inefficient migration of excitons to the heterojunction in this morphology. In the case of F8BT:PFB blend and F8TBT:P3HT pristine blend, it was only possible to obtain a lower limit for $\eta_A \times \eta_{ED}$, as the quantum efficiency was not found to saturate within the reverse bias range where $J-V$ curves remain stable (typically down to -5 V).

The parametrization of $\eta_{cc}(V)$ in terms of F_c is useful because it allows a direct and simple way of comparing geminate pair behavior in different devices. Before comparing the values extracted from experiment, we seek a microscopic interpretation of F_c. Equation 4 indicates that F_c depends on the recombination rate ν_r, and the dependence of carrier separation and extraction, $k_e(F)$, on electric field. For the latter, we turn to the theoretical description of charge separation formulated by Braun,[23] which has been successfully employed in the modeling of excitonic solar cells previously.[14] This indicates that $k_e(F) \propto \langle\mu\rangle r_c^2/r_0^3 \exp(-r_c/r_0) \times F$, where $\langle\mu\rangle$ is a combination of electron and hole mobility in the device on the length scale of carrier separation. r_c is the thermal capture radius $r_c = e^2/4\pi\varepsilon\varepsilon_0 kT$, and r_0 is the initial charge pair separation. These expressions may be combined to give

$$F_c \propto \frac{r_0^3 \nu_r}{\langle\mu\rangle r_c^2} \exp\left(\frac{r_c}{r_0}\right) \tag{7}$$

We can use this expression for F_c to investigate the influence both of morphology and of material properties on geminate pair dynamics. Of the devices investigated, three are composed of the same blend of materials, F8TBT and P3HT, see Figure 1. These devices were prepared to give different morphologies and indeed exhibit different values of the critical field as summarized in Table 1. The results yield several important insights into the role of morphology in affecting geminate pair behavior. The bilayer device exhibits a significantly smaller critical field than the as-spun blend device, illustrating the importance of heterojunction orientation with respect to the electric field. Annealing of the as-spun blend after cathode deposition reduces the critical field by an order of magnitude. This may be partially attributed to the blend coarsening that accompanies annealing, as this facilitates charge transport on the length scale of r_c. However, improved transport in the device owing to the well-known reorganization of P3HT under such conditions is likely also to contribute.[20]

In addition to morphology, it is clear from Table 1 that material properties strongly influence geminate pair behavior. Different material combinations exhibit very different critical fields, spanning more than 2 orders of magnitude. In particular, both fullerene blends investigated show very efficient charge separation. It should be noted that even in P3HT:PCBM devices, the $J-V$ characteristics here are determined by geminate recombination. In contrast, F8BT:PFB, a model PV system that has been extensively investigated, exhibits such inefficient charge separation that we can only give a lower bound for the critical field. The polymer:nanocrystal combination we investigate displays intermediate charge separation efficiency, but further hybrid blends must be analyzed to make a more general conclusion about nanocrystal performance.

We have proposed that F_c depends principally on the thermal capture radius r_c, the initial charge pair separation r_0, and the electron and hole mobility on the length scale of r_0, $\langle\mu\rangle$, see eq 7. Because we observe a very wide range of critical fields, it is natural first to examine which parameter may vary most widely between different materials. r_c depends principally on the dielectric constant of materials, which does not vary widely between the materials considered here. r_0 has not been measured experimentally in any system to date but may vary between different materials owing to differing degrees of charge wave function delocalization after charge transfer at the heterojunction.[24] However, the last factor, the mobility, is relatively simple to measure experimentally and is known to vary by several orders of magnitude among the materials investigated here. It should be noted that increased mobility and increased r_0 are related, as they can both result from improved charge delocalization.

There are several ways of measuring carrier mobility, including transistor characteristics, time-of-flight measurements, hole- and electron-only diodes based on pristine materials, and microwave conductivity.[25] However, it is apparent that charge transport in pristine films may be dramatically different from that in the blends with which we are concerned. Therefore, we make an estimate of carrier mobility specifically in our devices by fitting the quadratic region of the dark current under forward bias to a space-charge limited expression[26]

$$J_{e(h)} = \frac{9}{8}\varepsilon_0\varepsilon_r\mu_{e(h)} \exp\left(0.891\gamma_{e(h)}\sqrt{\frac{V}{L}}\right)\frac{V^2}{L^3} \tag{8}$$

This approach provides a reasonable estimate of the higher of the two materials' mobility in the blend in the case where transport is not well balanced. In Figure 3, we illustrate the strong correlation observed between the mobility determined in this way and the critical field. This is consistent with previous Monte Carlo simulations by the author,[27] which demonstrate the pronounced dependence of carrier separation efficiency on mobility. We emphasize that the bulk mobility plays a key role not because devices are transport limited but because the mobility quantifies also the rate of charge hopping away from the heterojunction and hence geminate pair separation. Transport on this nanometer scale should be understood in terms of hopping mediated by polaron wave function overlap and hence is related to the initial geminate pair separation. That this trend should apply across such a wide variety of material combinations is striking and strongly suggests that improved charge delocalization should be a primary goal in the development of improved materials for photovoltaics.

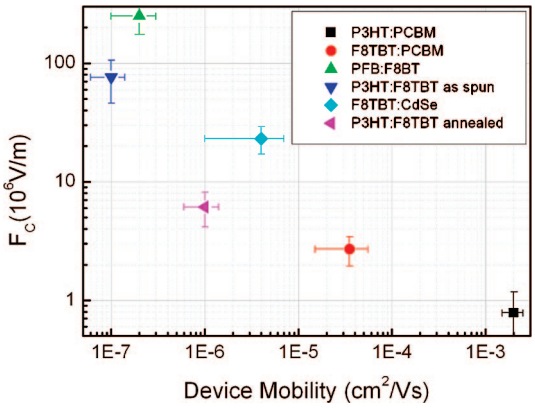

Figure 3. Comparison of the critical field extracted from different devices to their mobility, extracted by fitting a space-charge limited expression to the dark current at forward bias. This mobility is a measure of charge transport in the more mobile of the two constituent materials, taking into account the blend morphology. Therefore these mobilities do not necessarily correspond to those measured in pristine films.

Experimental Section. All devices comprise a bottom electrode of indium tin oxide (ITO) and a top electrode of aluminum. The ITO covered glass substrates were cleaned first using acetone and isopropyl alcohol then oxygen plasma treatment. PEDOT:PSS (40nm thick) was deposited by spin-coating onto the plasma-treated substrates and then annealed at 12 °C before being transferred to a nitrogen glovebox for further fabrication steps. The semiconducting layer was deposited by spin-coating in each case, see below for details. Each device was completed by the evaporation of 80 nm of aluminum at a pressure of less than 10^{-6} through a mask that defined an active area of 4.5 mm^2. Annealing of films and devices was carried out by placing substrates on a hot plate within the glovebox. All devices were encapsulated prior to testing. Current–voltage curves were obtained using monochromatic light, with a wavelength chosen in each case to maximize absorption (given below).

F8TBT:P3HT (as spun) device: 1:1 solution of total concentration 15 mg/mL prepared in xylene. Spin-coated at 3000 rpm to give a film thickness of 70 nm. Wavelength 550 nm.

F8TBT:P3HT (annealed) device: as above, and annealed after aluminum deposition at 140 °C. Wavelength 550 nm.

F8TBT:P3HT (bilayer) device: F8TBT dissolved in xylene at 10 mg/mL and spin-coated at 5000 rpm to give a 40 nm film. P3HT dissolved in cholorobenzene at 20 mg/mL and spin-coated at 2000 rpm to give a 40 nm film. Wavelength 575 nm.

F8BT:PFB device: 3:2 solution of total concentration 15 mg/mL prepared in chloroform. Spin-coated at 2000 rpm to give a film thickness of 100 nm. Wavelength 480 nm.

F8TBT:PCBM device: 1:3 solution of total concentration 20 mg/mL prepared in chloroform. Spin-coated at 1500 rpm to give a film thickness of 220 nm. Wavelength 550 nm.

P3HT:PCBM device: 1:1 solution of total concentration 22 mg/mL prepared in *ortho*-dichlorobenzene. Spin-coated at 600 rpm for 30 s and then allowed to dry in a covered petri dish to give a film thickness of 170 nm. Wavelength 600 nm.

F8TBT:CdSe device: CdSe branched nanorods of 50 nm length and 6 nm arm diameter were treated with pyridine to remove the surface ligand and dissolved in a 9:1 mixture by volume of chloroform:pyridine to give a concentration of 25 mg/mL. F8TBT was dissolved in trichlorobenzene at a concentration of 10 mg/mL. The two solutions were mixed to give a 1:6 ratio of F8TBT:CdSe and spin-coated at 1500 rpm to give a film thickness of 90 nm. Wavelength 560 nm.

Acknowledgment. R.A.M. thanks the George and Lilian Schiff Foundation and the EPSRC for financial support.

Note Added after ASAP Publication: There was an error in eq 1 in the version published ASAP March 26, 2008; the corrected version was published ASAP April 17, 2008.

Supporting Information Available: The raw data and fits used. This material is available free of charge via the Internet at http://pubs.acs.org.

References

(1) Sariciftci, N. S.; Braun, D.; Zhang, C.; Srdanov, V. I.; Heeger, A. J.; Stucky, G.; Wudl, F. *Appl. Phys. Lett.* **1993**, *62*, 585–587.
(2) Yu, G.; Gao, J.; Hummelen, J. C.; Wudl, F.; Heeger, A. J. *Science* **1995**, *270*, 1789–1791.
(3) Granstrom, M.; Petritsch, K.; Arias, A. C.; Lux, A.; Andersson, M. R.; Friend, R. H. *Nature* **1998**, *395*, 257–260.
(4) Kietzke, T.; Horhold, H. H.; Neher, D. *Chem. Mater.* **2005**, *17*, 6532–6537.
(5) McNeill, C. R.; Abrusci, A.; Zaumseil, J.; Wilson, R.; McKiernan, M. J.; Burroughes, J. H.; Halls, J. J. M.; Greenham, N. C.; Friend, R. H. *Appl. Phys. Lett.* **2007**, *90*, 193506.
(6) Kim, Y.; Cook, S.; Tuladhar, S. M.; Choulis, S. A.; Nelson, J.; Durrant, J. R.; Bradley, D. D. C.; Giles, M.; McCulloch, I.; Ha, C. S.; Ree, M. *Nat. Mater.* **2006**, *5*, 197–203.
(7) Zhou, Y.; Li, Y. C.; Zhong, H. Z.; Hou, J. H.; Ding, Y. Q.; Yang, C. H.; Li, Y. F. *Nanotechnology* **2006**, 17.
(8) Nelson, J. *The Physics of Solar Cells*; Imperial College Press: London, 2003.
(9) Ford, T. A.; Avilov, L.; Beljonne, D.; Greenham, N. C. *Phys. Rev. B* **2005**, *71*, 125212.
(10) Morteani, A. C.; Sreearunothai, P.; Herz, L. M.; Friend, R. H.; Silva, C. *Phys. Rev. Lett.* **2004**, *92* (24), 247402.
(11) Barker, J. A.; Ramsdale, C. M.; Greenham, N. C. *Phys. Rev. B* **2003**, *67*, 075205.
(12) Koster, L. J. A.; Smits, E. C. P.; Mihailetchi, V. D.; Blom, P. W. M. *Phys. Rev. B* **2005**, *72*, 085205.
(13) Koster, L. J. A.; Mihailetchi, V. D.; Ramaker, R.; Blom, P. W. M. *Appl. Phys. Lett.* **2005**, *86*, 123509.
(14) Mihailetchi, V. D.; Koster, L. J. A.; Hummelen, J. C.; Blom, P. W. M. *Phys. Rev. Lett.* **2004**, *93*, 216601.
(15) Nelson, J.; Choulis, S. A.; Durrant, J. *Thin Solid Films* **2004**, *451*, 508.
(16) Koster, L. J. A.; Mihailetchi, V. D.; Blom, P. W. M. *Appl. Phys. Lett.* **2006**, *88*, 052104.
(17) Tessler, N.; Rappaport, N. *Appl. Phys. Lett.* **2006**, 89.
(18) Koster, L. J. A.; Mihailetchi, V. D.; Xie, H.; Blom, P. W. M. *Appl. Phys. Lett.* **2005**, *87*, 203502.
(19) Slooff, L. H.; Veenstra, S. C.; Kroon, J. M.; Moet, D. J. D.; Sweelssen, J.; Koetse, M. M. *Appl. Phys. Lett.* **2007**, 90.
(20) Mihailetchi, V. D.; Xie, H. X.; de Boer, B.; Koster, L. J. A.; Blom, P. W. M. *Adv. Funct. Mater.* **2006**, 16.
(21) Mihailetchi, V. D.; Blom, P. W. M.; Hummelen, J. C.; Rispens, M. T. *J. Appl. Phys.* **1998**, *94*, 6849–6854.
(22) Kooistra, F. B.; Knol, J.; Kastenberg, F.; Popescu, L. M.; Verhees, W. J. H.; Kroon, J. M.; Hummelen, J. C. *Org. Lett.* **2007**, *9*, 551.
(23) Braun, C. L. *J. Chem. Phys.* **1984**, *80* (9), 4157–4161.

(24) Mandoc, M. M., Veurman, W., Sweelson, J., Koetse, M. M., Blom, P. W. M. *Appl. Phys. Lett.* **2007**, *91*, 073518.
(25) Coropceanu, V.; Cornil, J.; da Silva, D. A.; Olivier, Y.; Silbey, R.; Bredas, J. *Chem. Rev.* **2007**, *107*, 926.
(26) Murgatroyd, P. N. *J. Phys. D* **1970**, *3*, 151.
(27) Marsh, R. A.; Groves, C.; Greenham, N. C. *J. Appl. Phys.* **2007**, 101.

NL080200P